Observations of persistent Leonid meteor trails 3. The "Glowworm"

Jack D. Drummond,[1] Brent W. Grime,[1] Chester S. Gardner,[2] Alan Z. Liu,[2] Xinzhao Chu,[2] Michael C. Kelley,[3] Craig Kruschwitz,[3] and Timothy J. Kane[4]

Received 23 July 2001; revised 14 January 2002; accepted 14 January 2002; published 2 August 2002.

[1] A spectacular, well-observed Leonid meteor of visual magnitude −14.3 appeared on 17 November 1998 and left a lingering trail, dubbed the Glowworm, that was well studied. From a location on Kirtland Air Force Base, near Albuquerque, New Mexico, we obtained CCD images of the trail from 94 to 203 s after the meteor and recorded a video with an intensified camera for even longer. From information obtained with a sodium lidar half an hour after the meteor, we have determined that a gravity wave with a vertical wavelength of 2.4 km was responsible for the right-angled appearance of the trail. The trail ended abruptly at 85 km, and its uppermost altitude may have been no greater than 91 km. We designate the Glowworm a Type I trail: one that is wide (1 km), cloudy in appearance, has high diffusion rates (800 $m^2 s^{-1}$), high total line emission rates (1.5×10^{18} photons $m^{-1} s^{-1}$), and is optically thicker than Type II trails. The lower parts of the Diamond Ring, another Leonid lingering trail that appeared 38 min earlier than the Glowworm, define the Type II trails, which appear as narrow, optically thinner parallel trails, with low diffusion rates (12 $m^2 s^{-1}$) and total line emission rates ($1-3 \times 10^{16}$ photons $m^{-1} s^{-1}$). No explanation is offered for the two orders of magnitude difference in these quantities. The Glowworm meteor produced infrasound [*ReVelle and Whitaker*, 1999], from which a meteoroid mass estimate of 522 g was made. We compare our photometry to a detailed numerical modeling of the shape of the trail and emission from the Glowworm made by *Zinn et al.* [1999], who find that the largest contributors to emission recorded by our CCD and video cameras are atmospheric O_2 vibrational bands. Compared to our measurements, their calculated emission is too high by two orders of magnitude, but since most of O_2 emission may be absorbed by atmospheric O_2 before it reaches the ground, this may indeed be the primary contributor to the observed flux. Although the calculations of Zinn et al. lead to a hollow cylinder appearance which may be appropriate for the Glowworm, it is not pronounced enough to account for the complete darkness between the parallel structures seen in Type II trails. An upper limit to backscattering from dust of 3.7×10^{-5} of the expected return was found from directing a 180 W copper vapor laser at the Glowworm. *INDEX TERMS:* 0310 Atmospheric Composition and Structure: Airglow and aurora; 3384 Meteorology and Atmospheric Dynamics: Waves and tides; 6022 Planetology: Comets and Small Bodies: Impact phenomena; 6245 Planetology: Solar System Objects: Meteors; *KEYWORDS:* meteor, persistent meteor trails, comets, airglow, gravity waves, mesosphere

1. Introduction

[2] Continuing our study of lingering trails from Leonid meteors, we report on the brightest and most spectacular observed on 17 November 1998 from the Starfire Optical Range (SOR) on Kirtland Air Force Base, near Albuquerque, New Mexico. At 3:05:44 Mountain Standard Time (10:05:44 UT), a very bright meteor lit up the landscape and left a lingering trail, named the Glowworm, that was visible for 20 min to the naked eye, and to an all-sky sodium imager for more than an hour, as shown by *Zinn et al.* [1999] and *Kelley et al.* [2000]. Although the magnitude of the meteor was estimated by two local observers at the SOR as brighter than −4.5, this may have been a serious underestimate because they did not see the meteor directly, but based their estimate on the degree to which the landscape was flooded with light. Two other observers located in Los Alamos, NM, some 150 km north of the SOR, estimated the magnitude to be −10 [*ReVelle and Whitaker*, 1999], and a visual photometer recorded a brightness of −14.3 [*Zinn et al.*, 1999].

[3] Paper I [*Drummond et al.*, 2001] of our studies reported on the advection derived from the Diamond Ring,

[1]Starfire Optical Range, Directed Energy Directorate, Air Force Research Laboratory, Kirtland Air Force Base, New Mexico, USA.
[2]Department of Electrical and Computer Engineering, University of Illinois at Urbana-Champaign, Urbana, Illinois, USA.
[3]Department of Electrical and Computer Engineering, Cornell University, Ithaca, New York, USA.
[4]Department of Electrical Engineering, Pennsylvania State University, University Park, Pennsylvania, USA.

0148-0227/02/2001JA000223$09.00

a Leonid trail from a meteor that appeared 38 min earlier in the night, and paper II [*Kruschwitz et al.*, 2001] compared the photometry of the Diamond Ring to theoretical calculations and modelling. Additional observations of the Glowworm were reported from Los Alamos, NM, by *Zinn et al.* [1999], who also made detailed numerical calculations for the first 30 s of the fireball and subsequent trail. From infrasound recordings of the meteor's passage through the atmosphere over Los Alamos, *ReVelle and Whitaker* [1999] obtained a best estimate of 522 g for the meteoroid's mass, in agreement with the 526 g estimate from Zinn et al. In addition to papers I and II, our current paper on the Glowworm should be considered with the Zinn et al. and ReVelle and Whitaker papers in hand.

[4] Other reports on the Leonid trail campaign from the SOR are given by *Kelley et al.* [2000], *Chu et al.* [2000b], and *Grime et al.* [2000]. *Chu et al.* [2000a] also report on iron lidar studies of 1998 meteor trails. Excellent papers on similar campaigns can be found in the special issue of *Earth*, *Moon*, *and Planets*, edited by *Jenniskens et al.* [2000c]. In particular, *Jenniskens and Rairden* [2000] report an analysis similar to ours for the determination of wind and gravity wave parameters from a persistent train, and *Jenniskens et al.* [2000a] make an excellent study of the Chippenham persistent trail. We postpone a detailed comparison of our results and theirs until we have completed our analysis of two 1999 trails, the Puff Daddy and the French Curve, which will be the subject of future papers in our series.

[5] At the SOR, in addition to a 1 watt sodium lidar working through the 3.5 meter telescope, an intensified video camera was also attached to the superstructure of the telescope mount. At independent mounts, a CCD camera (0.5–1μm) was used to record images, and a 180 watt copper vapor laser was used in an attempt to produce backscatter from the trail. A visual observer called out altitude and azimuth information when a meteor was observed to leave a trail, and all mounts were able to train on the trail within 2 min [*Drummond et al.*, 2000].

[6] Figure 1 shows the vertical profiles of various parameters measured by the sodium lidar 33 min after the appearance of the Glowworm during its routine near-zenith pointing operations. The temperature variation with altitude shows a reversal exactly at the altitudes (see below) of the Glowworm, whereas the background sodium density is on the decline from its maximum. The magnitude and direction of the wind field as a function of altitude are shown in the bottom two plots of Figure 1. Notice that the wind direction changes from NW (−45°) to SW (−135°) as the altitude increases, but then reverses this trend at around 90 km. The wind velocity increases steadily at the altitudes of the Glowworm, but sharply decreases at 91 km. As shown by the open circles, which mark the altitudes of reference features in the Glowworm, these sharp gradients take place just at or above the top of our images.

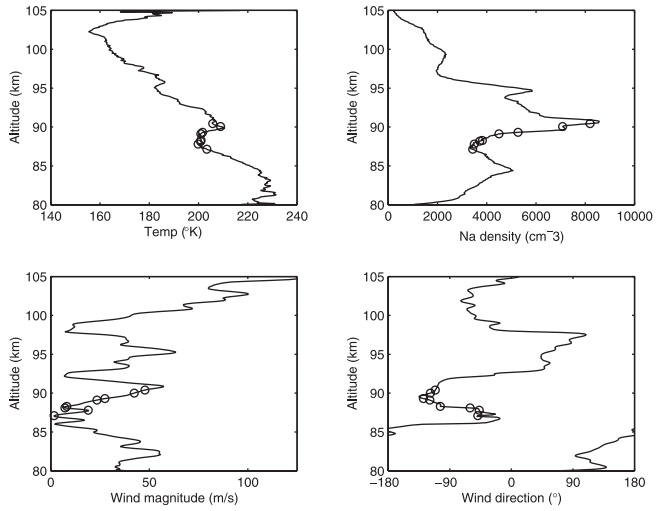

Figure 1. Vertical profiles of temperature, sodium density, and wind field at 10:36 UT, 17 November 1998, well away from the Glowworm itself. Between 80 and 95 km there is a 6° uncertainty in the temperature measurements and a 5% uncertainty in sodium density, both increasing slightly between 95 and 105 km altitude. Open circles mark the altitudes of the reference features on the images. The wind direction is measured with respect to North; +90° is eastwardly and −90° is westwardly.

2. The Diamond Ring Revisited

[7] Before we begin to address the Glowworm, we make some adjustments to the results for the Diamond Ring (papers I and II). For convenience, we designate wide, puffy, turbid, optically thicker trails as Type I, and narrow, (usually) parallel, optically thinner trails as Type II. In analyzing the Glowworm it was realized that the upper part of the Diamond Ring is a Type I trail, similar to the Glowworm, but the parallel Type II trail structure at lower altitudes in the Diamond Ring has no counterpart in the Glowworm.

[8] When intensity profiles (cuts) were made through the Diamond Ring at various places, mean geometric conditions were assigned to cuts 7 and 8 because they lay near the point of overlap of the trail where the lidar recorded return from two altitudes, 92.5 and 98 km. However, it now makes more sense to attribute most of the emission to a Type I trail at the higher altitude, since the trail has clearly achieved its Type II parallel, optically thin, low diffusion form by 92.5 km. Therefore, we repeat Table 2 from paper II in order to report the adjustments to cuts 7 and 8, and for comparison to the analysis of the Glowworm below.

[9] The Amplitude, Center, and σ in Table 1 are the Gaussian fit parameters of the cuts, the height and slant distance d are obtained from the sodium lidar and a geometric analysis of the trail, θ is the angle that the trail makes with the line of sight, also derived from the geometry of the perfect ellipse formed by the trail between 92.5 and 98 km altitude, l is the meters per pixel scale at the cut, and le_t is the total line emission per length of trail, more fully explained below. While cuts 1–6 were made perpendicular to the trail, cuts 7 and 8 were made at an angle of 45°, which is taken into account when computing le_t.

3. The Glowworm: Advection

[10] While a video and many CCD images were made of the Glowworm beginning 94 s (Figure 2) after the appear-

Table 1. Diamond Ring Gaussian Fit Parameters

Cut Number	Amplitude, photons s^{-1} m^{-2} $arcsec^{-2}$	Center, meters	σ, meters	Height, km	*d*, km	θ, deg	*l*, m pix^{-1}	$le_t \times 10^{16}$, photons s^{-1} m^{-1}
1	380 ± 49	450 ± 15	224 ± 37	96.86	124.1	42	8.3703	7.62 ± 1.77
2	283 ± 17	356 ± 8	163 ± 13	96.67	123.9	43	8.3582	4.23 ± 0.60
3	197 ± 47	221 ± 13	39 ± 19	95.08	123.6	48	8.3361	0.77 ± 0.42
	283 ± 50	574 ± 9	58 ± 13					1.64 ± 0.49
								2.41 ± 0.65
4	172 ± 28	260 ± 9	42 ± 11	94.94	123.5	47	8.3334	0.71 ± 0.23
	333 ± 22	640 ± 5	59 ± 7					1.93 ± 0.32
								2.64 ± 0.40
5	316 ± 30	226 ± 5	49 ± 6	93.75	122.1	45	8.2379	1.47 ± 0.27
	576 ± 34	472 ± 2	34 ± 3					1.86 ± 0.26
								3.33 ± 0.37
6	312 ± 33	270 ± 5	44 ± 5	93.51	121.6	48	8.2034	1.35 ± 0.26
	391 ± 28	527 ± 5	57 ± 5					2.20 ± 0.34
								3.55 ± 0.43
7	727 ± 77	685 ± 14	307 ± 37	98.00	126.2	50	8.5121	16.1 ± 3.06
	699 ± 58	1254 ± 7	72 ± 8					3.61 ± 0.61
	613 ± 155	1514 ± 11	66 ± 13					2.93 ± 1.00
	261 ± 86	1731 ± 78	138 ± 82					2.60 ± 1.79
								25.2 ± 3.73
8	750 ± 61	628 ± 15	260 ± 29	98.00	126.2	50	8.5121	14.0 ± 2.40
	723 ± 51	1197 ± 12	133 ± 12					6.94 ± 1.07
	342 ± 65	1514 ± 13	57 ± 14					1.42 ± 0.47
	331 ± 72	1787 ± 18	114 ± 29					2.72 ± 0.94
								25.1 ± 2.83

ance of the meteor, no altitude information was available for the trail from the lidar because the chopper wheel for the lidar was not set for such a low elevation. At 33° above the horizon the chopper gated out the return from the trail. However, *ReVelle and Whitaker* [1999] reported that triangulation measurements of visual and CCD observations placed the altitude of the Glowworm at 91 ± 7 km, while analysis of infrasound pressure wave data placed the source at 89.5 km.

[11] In this section we confirm their altitude estimates with an independent method. Our lidar measured the winds around the zenith in its normal routine stare operation mode half an hour after the appearance of the meteor, and by comparing the motion of features in the trail tracked by the CCD camera to the wind field found by lidar, a mean altitude estimate of 89 km for the Glowworm can be made, clearly lower than the Diamond Ring.

[12] Comparing the images and scale (derived below) to the video of the Glowworm, which shows the bottom of the trail not visible in any CCD image, it is estimated that the trail ends abruptly at around 85 km. The upper part of the trail, however, was seen by neither the CCD nor the video camera, and no estimate of its end height can be made. However, the long straight segment of the trail from the middle to the upper right, although it continues in the video beyond the edge of the frame in Figure 2, is perpendicular to the direction of the zenith, and if it never turns up may never reach altitudes greater than 91 km. Thus the uppermost altitude of the Glowworm is a soft 91 km, but the bottom is a hard 85.

[13] Figure 3 shows 16 images of the Glowworm from 94 to 203 s after the meteor. Across each image three cuts are made for the purpose of determining line emission rates (section 4) and diffusion rates (section 6). Each cut is made at right angles to the trail and an attempt is made to position them at the same place. The photometric center is determined and the root mean square (rms) distance from the center is plotted on each image in Figure 3. In addition to the three photometric centers, five more features are identified and tracked in the images. The image coordinates (with respect to the stars) of these 8 features in the Glowworm can be expressed as a linear function of the 16 times to find their location at time zero.

[14] Because the parent meteor is a Leonid, its atmospheric trajectory through the field of the camera is known in this direction, and can be drawn through the mean positions of the eight time zero points. The intersections of the eight individual lines of motion and the reference trajectory are then used as the true zero points. It remains to determine the distance of these true zero points from the camera in order to transform the image coordinates to true coordinates, but by assuming that there is little vertical motion (as confirmed by vertical wind measurements with lidar during the course of the night), the same altitude can be assigned to each feature at all 16 times. Dividing the difference between each distance and its intersection by the time interval yields the 'image winds'. This image wind field can then be rotated to the true wind field by adopting a mean distance to the trail.

[15] The wind field from the lidar 33 min later is plotted in Figure 4 as a function of altitude, as are the 8 individual *U* (eastwardly) and *V* (northwardly) components. Sliding the transformed winds vertically, the best match (in a least

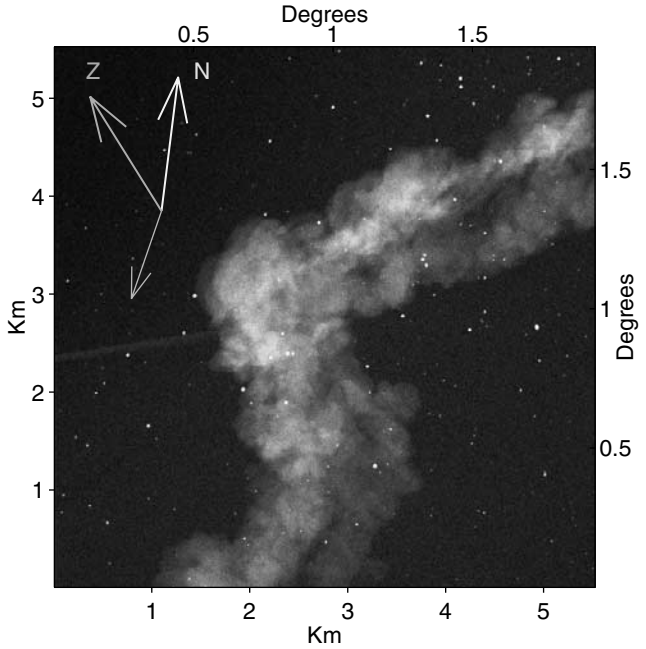

Figure 2. The Glowworm. Ninety four seconds after the appearance of the fireball at 3:05:44 MST, the first one s exposure of its lingering trail was made. The center of the image is directed at an elevation of 33° and an azimuth of 358°. The direction to the zenith and celestial north is indicated, with azimuth increasing to the right, 90° clockwise from the direction to the zenith. The unmarked arrow represents the direction and length of the projection of one kilometer of the initial trail. Barely visible coming in from the left edge is the laser of the 1 watt sodium lidar. See color version of this figure at back of this issue.

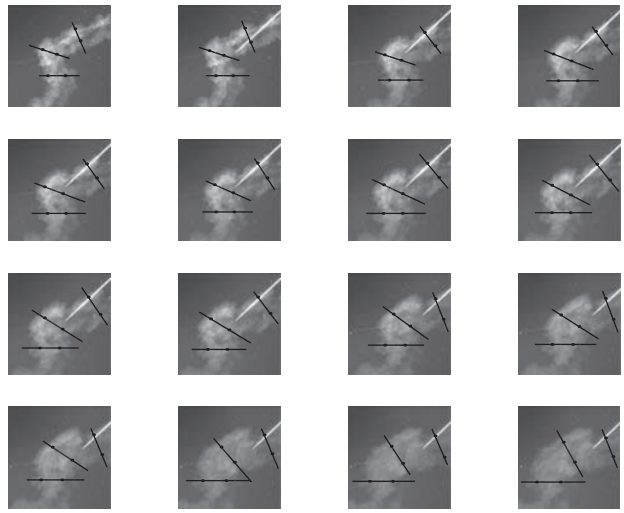

Figure 3. Cuts across 16 images of the Glowworm. The times of each image after the appearance of the meteor are from left to right, top to bottom: 94, 101, 116, 117; 118, 120, 121, 123; 124, 125, 173, 175; 176, 199, 201, 203 s. Cut 1 is the middle one, cut 2 is the one at bottom, and cut 3 is the one at upper right in each image. Dots mark the rms edges. The 1 watt sodium lidar can be seen coming in from the left edge in most frames, and a 180 watt copper vapor laser is coming in from the upper right in all but the first frame.

squares sense) to the lidar winds occurs for a mean altitude of 88.8 km.

[16] Adopting the altitude information derived from lidar measurements of the wind field some 33 min after the Glowworm's appearance, we can search for a dominant gravity wave that might be responsible for the distinctive right angles in the trail. Earlier in the evening, a monochromatic gravity wave with a vertical wavelength of 5.5 km and a horizontal wavelength of 2650 km was found from an analysis of the Diamond Ring (paper I) which appeared at 2:28 MST. This wave was found at altitudes between 92.5 and 98 km, but the kinks in the Glowworm are evidently at lower altitudes. In order to find the properties of the gravity wave responsible for the appearance of the Glowworm, we make a simultaneous fit of the wind field in m s^{-1} for each time with equation (1), where Z is altitude in km:

$$U = A_x + B_x Z + C_x \cos[(Z - Z_{0x})2\pi/\lambda]$$
$$V = A_y + B_y Z + C_y \sin[(Z - Z_{0y})2\pi/\lambda] \quad (1)$$

[17] Rather than show the results for all 16 fits, we show four frames in Figure 5. Notice the kink in the Glowworm, especially in the first frame, caused by a strong wind gradient. The only place where a similar feature can be produced by the lidar winds is at the adopted altitude, although the observed kink in the images of Figure 5 is somewhat below what would be produced by the lidar wind (dashed line) determined 33 min later.

[18] The 16 fits for the 16 times indicate that the wind field is not static, but varies slightly around a mean wind

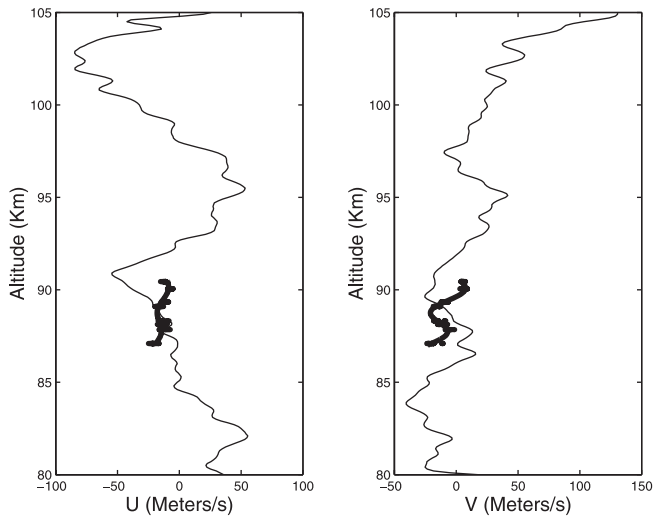

Figure 4. The wind field as determined by lidar 33 min after the Glowworm observations. Positive U corresponds to the eastward component, and V to the northward component. The 16 different wind determinations for each of the eight reference features run together at their 8 respective altitudes. By sliding these points up and down, in a least squares sense, it is determined that the mean altitude for the image is 88.8 km. Also plotted as a thicker line is the mean wind from the global fit.

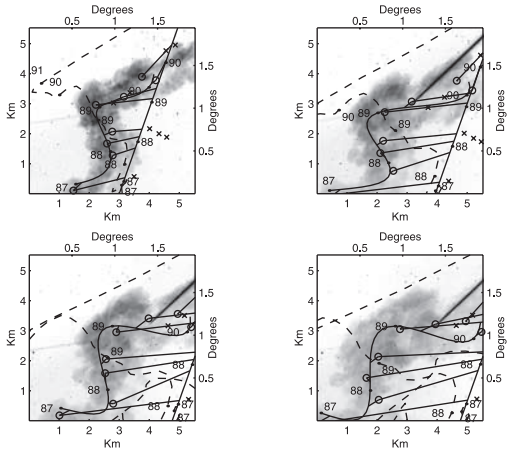

Figure 5. The results from fitting the wind field for a gravity wave at four times. The top two images were made 94 and 125 s after the meteor, and the bottom two were taken 173 and 203 s after the meteor. Superimposed on each image are the positions of the eight features (o) used to derive the wind at that altitude, the straight line paths from their point of origin on the initial trajectory, the time zero points (x, which either lie on the path or on its extension), and the location of the trajectory (dashed line) if the lidar wind were acting for the appropriate length of time. The curved solid line is the result of the wind derived with equation (1) on the trajectory, and each point is connected to its predicted position on this line. Altitudes in kilometers are indicated.

field derived from making a global fit of all 128 U and 128 V determinations. Table 2 gives the coefficients and their uncertainties from this global fit, and Figure 6 shows the individual wind fields at each time. Separating the individual winds by displacing them horizontally by their time since ablation results in Figure 7, which better shows how the wind field changes around the mean over time.

[19] The gravity wave vertical wavelength of 2.36 ± 0.02 km that we find for the Glowworm is about half of what was observed for the Diamond Ring 38 min earlier, but the region, 87.1–90.4 km, over which it was determined is lower than the 92.5–98.0 km range of the Diamond Ring. From a study of a persistent trail over Corsica in the Mediterranean Sea on 18 November 1999, *Jenniskens and Rairden* [2000] find a gravity wave vertical wavelength of 8.3 ± 0.5 km, as determined over an altitude range of 79–91 km, with an amplitude of 57 ± 8 m s^{-1}. The amplitude of $\sqrt{C_x^2 + C_y^2} = 10.9 \pm 0.5$ m s^{-1} for the Glowworm and of 23.0 ± 0.2 m s^{-1} for the Diamond Ring are lower, perhaps because we allowed a vertical wind gradient in addition to the gravity wave. The 2.4–8.3 km range of vertical wavelengths are

Table 2. Equation (1) Wind Parameters as a Function of Altitude

Coefficient	U, m s^{-1}	V, m s^{-1}	Units
A	−230 ± 19	−556 ± 19	m s^{-1}
B	2.36 ± 0.02	6.1 ± 0.2	m s^{-1} km^{-1}
C	3.1 ± 0.4	10.4 ± 0.5	m s^{-1}
Z_0	90.03 ± 0.04	89.42 ± 0.01	km
λ	2.358 ± 0.022	2.358 ± 0.022	km

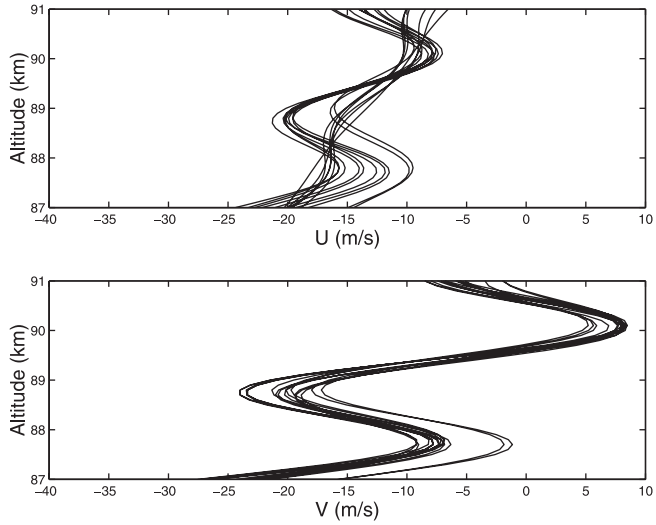

Figure 6. Wind field vs altitude. The wind components as derived with equation (1) at each time are shown as a function of altitude.

illustrative of the type of gravity waves that may be studied with persistent trails in the 70–100 km altitude range.

4. The Glowworm: Photometry

[20] The 16 frames of the Glowworm were photometrically calibrated by measuring the same half dozen stars in each frame and comparing their counts to their expected blackbody flux. The three intensity profiles in each frame were then converted to flux density in photons per second per square meter, and divided by the pixel size $(13.91'')^2$ to give the surface brightness, *sb*, across the trail in photons

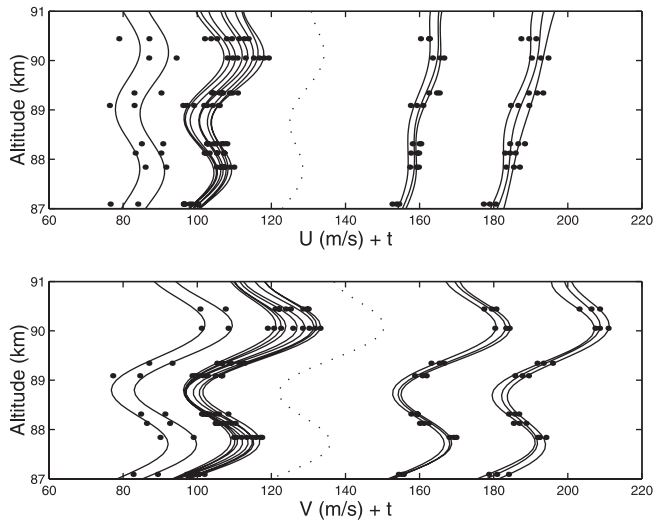

Figure 7. Wind field vs altitude as a function of time. To better reveal how the wind changes with time, the individual curves of Figure 5 are displaced horizontally by their time since ablation, t. The dots are the individual wind determinations for each time and altitude and the dotted line shows the mean wind derived from the global fit, plotted at the mean time of all the images.

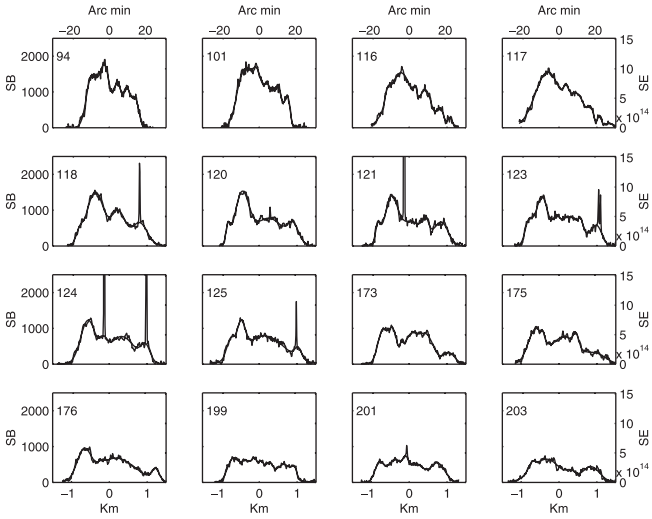

Figure 8. Surface brightness and surface emission for cut 1. The time in seconds since ablation is indicated in each plot. Surface brightness in photons s^{-1} m^{-2} $arcsec^{-2}$ is indicated on the left axis and the surface emission at the source in photons s^{-1} m^{-2} is indicated on the right scale.

per second per square meter per square arc second. The intensity profile (*sb*) of each cut was fit as a series of Gaussians on a local background. Figure 8, Figure 9, and Figure 10 show the profiles and the Gaussians for cuts 1–3, respectively, where the spikes are either due to stars, or for cut 3, the copper vapor laser. The left-hand scale shows the surface brightness while the right-hand scale shows the surface emission, *se*, at the source

$$se = 4\pi d^2 \sin\theta \, sb \frac{13.91^2}{l^2} \, [\text{photons s}^{-1}\text{m}^{-1^2}] \qquad (2)$$

where the d is the distance to the trail, θ is the angle between the trail and our line of sight (known because the initial trajectory and subsequent changes caused by the winds were calculated in the last section), and l is the length of a pixel at the source in meters.

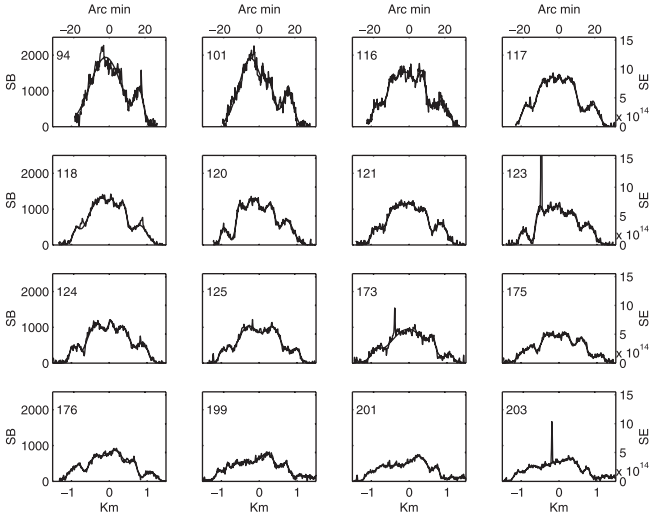

Figure 9. Same as Figure 8, but for cut 2.

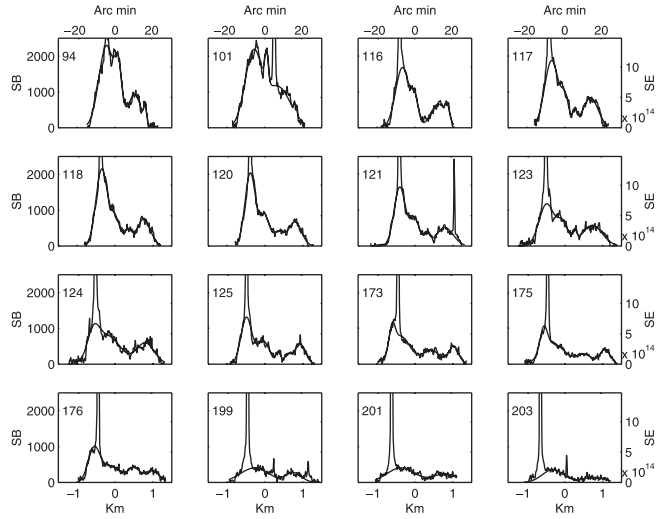

Figure 10. Same as Figure 8, but for cut 3.

[21] The total line emission per length of trail, le_t, can be found be simply integrating *se* across the width of the trail, which for the series of Gaussians is merely the sum of their areas

$$le_t = 4\pi d^2 \sin\theta \frac{13.91^2}{l^2} \, \Sigma(A\sqrt{2\pi}\sigma) \quad [\text{photons s}^{-1}\,\text{m}^{-1}] \qquad (3)$$

where A is an individual Gaussian amplitude and σ is an individual rms. Figure 11 shows the decay of the total line emission rate with time. In the range of the data, 94–203 s, it is not possible to distinguish among fits of le_t to the 0.5, 1, and 2 powers of time, or to an exponential decay with time, so we only show the linear and exponential decay fits in Figure 11.

[22] The linear decay rates are 4.0 ± 0.5, 5.2 ± 0.6, and $6.2 \pm 0.8 \times 10^{15}$ photons m^{-1} s^{-2}, from initial linearly projected total line emission rates of 1.37 ± 0.07, 1.57 ± 0.09, and

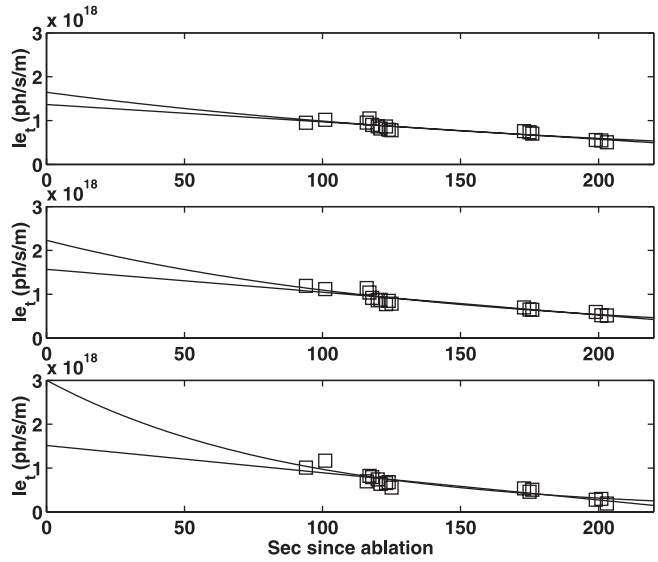

Figure 11. Decay of le_t with time. Cut 1 at 89.1 km altitude is at the top, Cut 2 at 88.1 km is in the middle, and cut 3 at 90.4 km is at the bottom. The lines show a linear and an exponential decay rate.

$1.51 \pm 0.11 \times 10^{18}$ photons m^{-1} s^{-1}. This simple linear decay is in contrast to a more complicated decay exhibited by another trail reported by *Jenniskens et al.* [2000a]. If, as they assume, the decay is exponential with time then, for cuts 1–3, the decay constants are 196 ± 27, 141 ± 16, and 87 ± 12 s for initial emission rates of le_t = 1.6 ± 0.2, 2.2 ± 0.2, and 3.0 ± 0.6 × 10^{18} photons m^{-1} s^{-1}, respectively. Our decay rates are comparable to their range of 63–190 s between 86 and 96 km altitude, but they find a trend with altitude that we do not see, probably because of the small range of our altitudes (88.1–90.4 km).

5. Scattering From Dust

[23] The 180 watt copper vapor, operating at 0.511 microns, dominates most of the images in Figure 3. Focused at 10.5 km distance, it produced 0.16 W m^{-2} over a 22 m diameter footprint at the 165 km distance of the Glowworm, covering 2X2 CCD pixels. By running the images together in a movie, and by carefully inspecting the video, no return signal from the laser could be detected. The mean of 16 standard errors of fit for cut 1 in the vicinity of the expected return is 91 photons m^{-2} s^{-1} $arcsec^{-2}$. Using three times this as a threshold for a return signal detection, an upper limit to the surface brightness of a spot produced by scattering (from dust) from the Glowworm can be set at 273 photons m^{-2} s^{-1} $arcsec^{-2}$. If the Glowworm reflected 100% of the photons from the laser into 4π steradians, then the surface brightness of the spot would have been 7.4 × 10^6 photons m^{-2} s^{-1} $arcsec^{-2}$. Thus less than 3.7×10^{-5} of the expected light from a perfect scatterer is seen.

6. The Glowworm: Diffusion Rates

[24] We adopt the classical form for the diffusion rates D of the lingering trail as a function of time

$$\overline{r^2} = 2Dt + \overline{r_0^2} \tag{4}$$

where $\overline{r^2}$ is the mean squared distance from the center μ, and $\overline{r_0^2}$ is for the time of ablation, time zero. This assumption is justified for the following reasons: 1) The integrated line emission rate derived in section 4 decays slowly in 200 s, indicating that the observed expansion of the trail may be a conserved tracer of diffusion, with little change due to chemical evolution; 2) The model developed in paper II of our series also shows no decrease in the total line emission rate because in the single dominant source of emission, the catalytic sodium reaction with ozone (see section 9), there is no sink for sodium and the ozone is barely depleted; 3) Most of the multiple Gaussians used to describe the trail in section 4 can be followed from frame to frame, and are consistent with simple expansion due to diffusion.

[25] For a cut across a trail that can be fit as a single Gaussian with a standard deviation σ and center μ, $\sigma^2 = \overline{r^2}$, and equation (4) is the same as equation (1) in *Chu et al.* [2000a]

$$\sigma^2 = 2Dt + \sigma_0^2 \tag{5}$$

where σ_0 is for time zero.

[26] For cuts across trails like the Glowworm, which are composed of multiple Gaussians,

$$\overline{r^2} = \frac{\Sigma(r^2 G)}{\Sigma G} - \left(\frac{\Sigma(rG)}{\Sigma G}\right)^2 \tag{6}$$

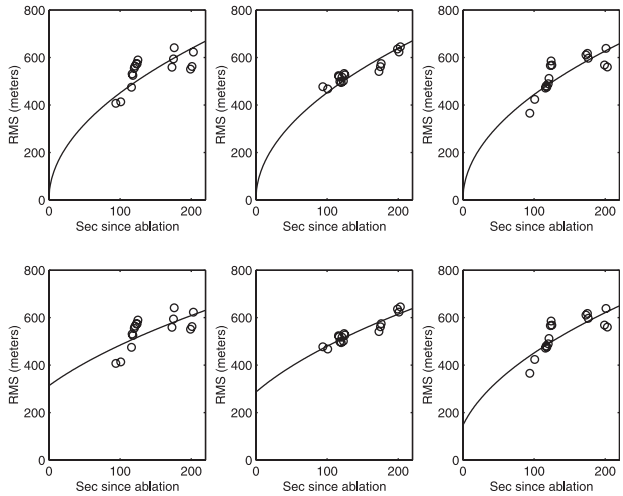

Figure 12. Diffusion as a function of time. Individual fits to the three cuts (left to right) with an intercept of zero at time zero are at the top, and fits with the intercept as free parameters are at the bottom.

where the term on the right is μ^2, and where G represents at each point the sum of the series of individual Gaussians G_i (with σ_i and μ_i) fit to each cut at each time. In terms of the individual Gaussians that comprise the trail, equation (6) can also be written as

$$\overline{r^2} = \frac{\Sigma(\sigma_i^2 G_i)}{\Sigma G_i} - \frac{\Sigma(\mu_i^2 - \mu^2) G_i}{\Sigma G_i} \tag{7}$$

[27] Figure 12 shows the results for each cut from the fits with equation (4) of $\overline{r^2}$ to the sixteen times, assuming both a non-zero and zero size at time zero. Cuts 1–3 yield diffusion rates in m^2 s^{-1} of 1017 ± 53, 1021 ± 26, 985 ± 44, for an intercept of zero at time zero, or 681 ± 190, 740 ± 76, 911 ± 176, for initial rms sizes of 313 ± 86, 286 ± 37, and 146 ± 168 meters, respectively.

[28] Since the trail undoubtedly suffered an initial violent expansion from a shock wave, it is not appropriate to assume for the wide Glowworm that classic diffusion began with an initial size of zero at time zero. By the time of our first image however, the effects of the shock wave will have dissipated, and the trail will be in a state of classical diffusion. Therefore, we adopt the non-zero intercept case for diffusion without specifying the details of the expansion before the first image. In order to find a common zero intercept that may apply to other situations, such as the Diamond Ring where only one image was taken, we fit all of the Glowworm data simultaneously and find an average initial size of σ_0 = 255 ± 49 m, and its associated single diffusion coefficient of D = 783 ± 90 m^2 s^{-1}.

7. Diffusion: Combining the Diamond Ring and the Glowworm

[29] Diffusion rates can also be calculated for the Diamond Ring observed 38 min earlier, but since only one CCD image was obtained 82 s after the appearance of the meteor, equation (5) reduces to $D = \sigma^2/164$ for an assumption of $\sigma_0 = 0$, where σ is taken directly from Table 2 for single Gaussians (cuts 1–6). Whether the fitted σ or half the

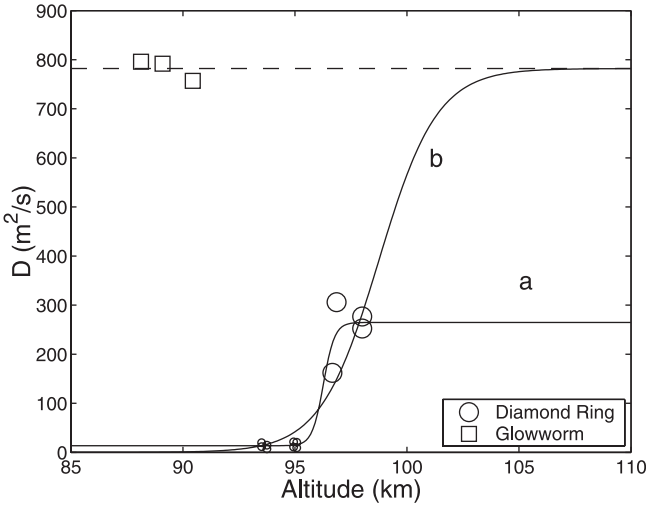

Figure 13. Diffusion as a function of altitude. The eight smallest diffusion coefficients for the Diamond Ring, shown as small circles, are characteristic of Type II trails, while the Glowworm squares are clearly Type I. The dashed line is the adopted upper limit to D, determined from the Glowworm. The solid lines *a* and *b* are the two hyperbolic tangent fits discussed in the text.

distance between the Type II parallel trails is used as a measure of the size of the trail, both are smaller 82 s after ablation for cuts 1–6 than the σ_0 of 255 m found in the last section. It appears that these portions of the trail may have begun diffusing from a near zero size near time zero.

[30] While the upper part of the Diamond Ring is like the Glowworm, a Type I trail, turbid, with high diffusion rates, the lower part, appearing as two parallel trails with much lower diffusion rates, is Type II. Treating each of the lower altitude parallel trails separately, the average of eight diffusion rates from cuts 3–6 is $D = 12 \pm 2$ m^2 s^{-1}. *Grime et al.* [2000] reported $D = 10 \pm 5$ m^2 s^{-1} for the Diamond Ring, derived from the width of the lidar return after several minutes, and for two other trails the same night they found $D = 8 \pm 3$ m^2 s^{-1} and $D = 5 \pm 2$ m^2 s^{-1}. The latter, 5 m^2 s^{-1}, is the diffusion rate used in paper II for the Diamond Ring. All assumed negligible size at time zero.

[31] For higher altitude cuts 1 and 2 of the Diamond Ring, before it appears double, the rms sizes are still greater than 255 m, and so the diffusion rates are again calculated from equation (5) with $\sigma_0 = 0$, yielding 306 and 162 m^2 s^{-1}, respectively. At still higher altitudes the trail is Type I and larger than 255 m. Therefore, we use equation (4), with $r_0^2 = 255^2$, for cuts 7 and 8, where their rms values, calculated with equation (6), are multiplied by sin 45° to make them perpendicular to the trail at the 98 km height after 82 s. This yields an average $D = 274 \pm 11$ m^2 s^{-1} for the two cuts at the same 98 km altitude.

[32] Figure 13 shows the individual diffusion rates plotted as a function of altitude for both the Glowworm and the Diamond Ring, which prompts us to attempt to make a global fit with the hyperbolic tangent function:

$$D = A + B \tanh\left(\frac{z - z_0}{H}\right) \quad (8)$$

Table 3. Equation (8) Coefficients for Diffusion

	Case a	Case b
A, m^2 s^{-1}	134 ± 4	391 ± 45
H, km	0.53 ± 0.25	2.51 ± 0.41
z_0, km	96.35 ± 0.20	98.62 ± 0.23
B, m^2 s^{-1}	147 ± 3	391
Se, m^2 s^{-1}	8	36

The asymptotes are $D = A + B$ and $D = A - B$. Thus if $B = A$ in equation (8), then one of the asymptotes is $D = 0$ and the other is $D = 2A$. The extension of the tangent of the *tanh* curve at the midpoint, $z = z_0$, intercepts the asymptotes at $z = z_0 - H$ and $z = z_0 + H$. Thus H is a scale length; three fourths (0.76) of the range of D occurs between $z_0 \pm H$. The hyperbolic tangent function is a purely heuristic mechanism to illustrate the transition from one state to another, and is not based on any physical model.

[33] The results from two fits with equation (8) are shown with the data in Figure 13, and the coefficients from the fits are given in Table 3 along with the standard error of each fit. Curve *a*, with the lower asymptote in Figure 13, shows the fit with only the Diamond Ring data, while curve *b*, with the higher asymptote, shows the fit of the Diamond Ring data under the assumption that the D (782 m^2 s^{-1}) from the Glowworm represents the asymptote, and where A is forced to equal B (the lower asymptote is forced to be zero). For case *a* the lower asymptote is $D = 13 \pm 4$ m^2 s^{-1}.

8. Line Emission: Combining the Diamond Ring and the Glowworm

[34] Just as was done for the diffusion rates, if we assume that the mean of the Glowworm total emission rates extrapolated linearly to 82 s after ablation represents the

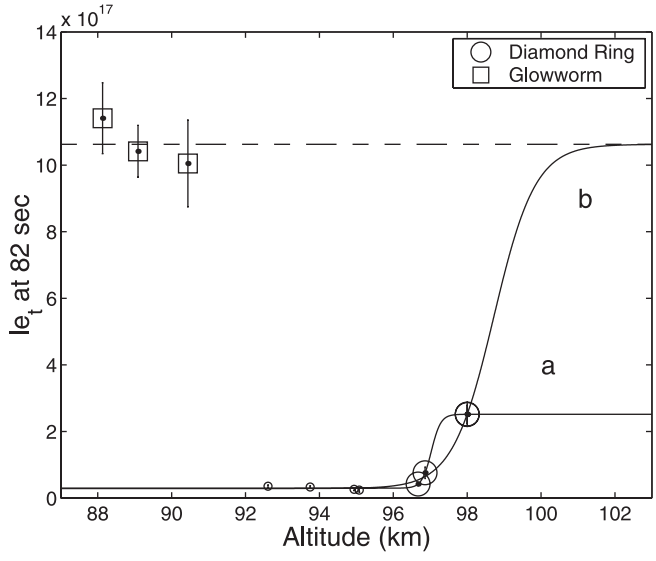

Figure 14. Total line emission rates 82 s after ablation as a function of altitude for the Diamond Ring and Glowworm. Curve *a* shows a *tanh* fit to the Diamond Ring only, and curve *b* shows the fit to the Diamond Ring data assuming that the mean Glowworm le_t is the upper asymptote (dashed line).

Table 4. Equation (8) Coefficients for le_t

	Case a	Case b
A, $\times 10^{17}$ photons m^{-1} s^{-1}	1.11 ± 0.02	5.17 ± 0.05
H, km	0.25 ± 0.08	1.12 ± 0.13
z_0, km	97.03 ± 0.06	98.72 ± 0.09
B, $\times 10^{17}$ photons m^{-1} s^{-1}	1.41 ± 0.02	5.46 ± 0.05
Se, $\times 10^{15}$ photons m^{-1} s^{-1}	4.73	8.96

upper asymptote for the *tanh* function, then Figure 14 curve *b*, shows the results. Curve *a* shows the fit without the Glowworm. Table 4 gives the coefficients for the fit to equation (8), with le_t substituted for *D*, and *B* not forced to equal *A*.

9. Discussion

[35] Table 5 summarizes the results for the three cuts through the Glowworm. For comparison to the Type I part of the Diamond Ring, quantities in the table are calculated for 82 s after ablation, even though this is 12 s before the time of the first Glowworm image. The rms size of the trails at 82 s comes from equation (4) using the non zero intercept diffusion rates of section 6, and the emission rate is from a linear extrapolation.

[36] For the Diamond Ring 82 s after ablation, the rms size for cuts 7 and 8, the widest part of the trail at the highest altitudes (98 km), are 332 and 326 meters, respectively, and as reported in section 7, the mean diffusion rates for these two cuts is $D = 274 \pm 11$ m^2 s^{-1} for $\sqrt{\overline{r_0^2}} = 255$ m.

[37] If, as we tried to show, the total line emission rate, and especially the diffusion, for the Glowworm can be related to the Diamond Ring, then the Type II trail phenomena of narrow, optically thin, parallel trails with low diffusion rates (12 m^2 s^{-1}) that occur below 95 km for the Diamond Ring is absent or masked in the Glowworm, even though the Glowworm is between 85 and ~91 km. Alternatively, the formation of a Type II trail instead of a broad, optically thick trail with high diffusion rates (Type I trail) may represent a different process than evident in the upper parts of the Diamond Ring or over the entire length of the Glowworm.

[38] The final appearance of a Type I or II trail may ultimately depend on two (or more) competing processes, with the Glowworm illustrating the total dominance of one process, and the Diamond Ring showing both. The transition between one process dominated region and the other, when they both exist, can apparently be described with the hyperbolic tangent function, since both diffusion and total line emission for the Diamond Ring show a smooth trend from low to high rates (Type II to Type I), and can be extrapolated to the higher diffusion and emission rates observed for the Type I Glowworm. Taking the weighted mean of the *tanh* function scale length, *H*, and the midpoint of the transition region between Type I and Type II trails, z_0, for the case *b* diffusion and le_t studies gives $z_0 = 98.71 \pm 0.03$ km and $H = 1.25 \pm 0.4$ km, for the night of 17 November 1998 over Albuquerque, New Mexico.

[39] The sodium catalytic reaction with ozone produces emission from sodium and from O_2 electronic and vibrational transitions

$$Na + O_3 \rightarrow NaO + O_2$$

$$NaO + O \rightarrow Na^* + O_2^*$$

since these reactions are exothermic. The O_2^* emission includes contributions from the $O_2(b^1\Sigma_g^+)$ to $O_2(X^3\Sigma_g^-)$ transitions, which produce vibrational bands between 0.7 and 0.9 μm, in the middle of the pass band for both our CCD and video cameras. However, the largest contribution to emission from the numerical modelling of the Glowworm by *Zinn et al.* [1999] are from the O_2 bands produced by recombination of disassociated oxygen

$$O(^1D) + O_2 \rightarrow O + O_2(b^1\Sigma_g)$$

Recently obtained spectra of persistent trains either do not cover this region [*Jenniskens et al.*, 2000b] or are too noisy here [*Borovička and Jenniskens*, 2000]. This O_2 emission was calculated by Zinn et al. to have a peak surface emission rate of $se = 5 \times 10^{17}$ photons m^{-2} s^{-1} 10 s after ablation, in regions 180 to 400 m on each side of the axis (a hollow cylinder profile). Linearly extrapolating our le_t in Figure 11 to 10 s gives a mean of around 1.5×10^{18} photons s^{-1} m^{-1} for the three cuts, and dividing this by $\sqrt{2\pi}\sigma$, where $\sigma = 284$ m is the extrapolated rms of the trail at 10 s, gives a mean observed peak surface emission of 2×10^{15} photons m^{-2} s^{-1}, 20 times less than calculated by Zinn et al. Note, however, that the area of a series of Gaussians is not equal to $\sqrt{2\pi}$ times the extrapolated size from the diffusion equation (unless the second term in equation (7) vanishes), but only serves to illustrate the order of magnitude of our peak surface emission.

[40] In the Zinn et al. model, treating the region between 180 and 400 m from the axis as a rectangle, then multiplying their *se* by twice 220 m gives a total line emission rate of $le_t = 2.2 \times 10^{20}$ photons m^{-1} s^{-1}, 150 times greater than our mean at 10 s of 1.5×10^{18}. Because atmospheric O_2 will absorb photons from transitions that terminate on the vibrational ground state, most, if not all, of the emission from the O_2 bands will not reach the ground. Thus the apparent disagreement of 20–150 times may not be as bad as it appears, lending support to the theory that the dominant contributor to the CCD images may indeed be from excited diatomic oxygen.

Table 5. Results for Glowworm Intensity Profiles

	Cut 1	Cut 2	Cut 3
Altitude, km	89.1	88.1	90.4
Initial total line emission rate, 10^{18} photons m^{-1} s^{-1}	1.40 ± 0.07	1.58 ± 0.10	1.55 ± 0.12
Total line emission rate decay, 10^{15} photons m^{-1} s^{-2}	4.1 ± 0.5	5.2 ± 0.7	6.4 ± 0.8
Total line emission rate at 82 s, 10^{18} photons m^{-1} s^{-1}	1.0 ± 0.1	1.1 ± 0.1	1.0 ± 0.1
Diffusion rate, m^2 s^{-1}	681 ± 190	740 ± 76	911 ± 176
RMS size at 82 s, m	458 ± 68	451 ± 27	413 ± 69

[41] The Type II double trail appearance of portions of the Diamond Ring, and of parts of most other trails from this night, still remains a mystery. As also addressed by *Jenniskens et al.* [2000a] and paper II, the empty appearance between the trails does not support the limb brightened, hollow cylinder model, caused by chemical depletion in the central region, but instead suggests two independent trails which may have formed subsequent to ablation from a near zero size. However, since the Glowworm is strictly a Type I trail, the hint of a dark spine down the middle of the length of its trail, especially evident in the video, may be the remnant of the hollow cylinder model that Zinn et al. predict up through 30 s after ablation, at which point their calculations stop. Perhaps sometime before the first image of the Glowworm taken at 94 s, this hollow cylinder may have filled in.

10. Summary

[42] We designate the wide, turbid, optically thick lingering trails with high diffusion and high line emission rates as Type I trails. The narrow, optically thin, usually parallel trails with low rates are designated as Type II. The Glowworm, a lingering trail from a Leonid meteor is strictly a Type I, while the Diamond Ring, observed 38 min earlier in the night, exhibits both types of trails. Although the two types of trails may indicate two or more processes taking place, at this point we have no explanation for the two orders of magnitude difference in both diffusion and line emission rates between them. After we complete an analysis of our two remaining trails, we intend to compare all of our trails to the Y2K [*Jenniskens and Rairden*, 2000] and Chippenham [*Jenniskens et al.*, 2000a] trails, and any others that become available, in order to gain some insight into the Type I and II phenomena.

[43] By comparing the wind field derived from tracking the motion of 8 reference features in 16 images of the Glowworm to the wind field found with a sodium lidar 33 min later, its altitude is found to be between 85 and $\sim$ 91 km. The kinks in the trail show the effects of a gravity wave with a vertical wavelength of 2.4 km.

[44] High initial total line emission rates (1.5×10^{18} photons s^{-1} m^{-1}) that remain high (1.0×10^{18}) for the Glowworm 82 s after ablation, as well as high diffusion rates (800 m^2 s^{-1}), can be connected with the hyperbolic tangent function to the much lower values for the Type II trail in parts of the Diamond Ring ($1-3\times10^{16}$ photons s^{-1} m^{-1} at 82 s and 12 m^2 s^{-1}, respectively).

[45] The maximum emission predicted for the Glowworm by Zinn et al. at 10 s after ablation are from O_2 vibrational bands. Too high by two orders of magnitude, much of this emission would be absorbed by atmospheric O_2 before a ground based observer could record it, and thus, in the end, may account for the majority of light detected by the 0.5–1 μm pass band of our CCD camera. Emission from other species, such as NO_2 ($le_t = 1.5 \times 10^{17}$) and O ($8 \times 10^{16}$) photons m^{-1} s^{-1}, are too low by at least an order of magnitude to the emission (1.5×10^{18}) extrapolated from our photometry of our images to 10 s after ablation, with sodium emission even fainter (paper II).

[46] The hollow cylinder appearance predicted by Zinn et al. is not pronounced enough to explain Type II trails observed in parts of the Diamond Ring, but may, if it fills in by 94 s after ablation, account for the overall appearance of the Glowworm. Type II parallel trails remain unexplained. No scattering from a 180 w copper vapor laser directed at the Glowworm was detected.

[47] **Acknowledgments.** We appreciate the thorough reviews made by two referees, which materially improved the paper. We thank the staff of the Starfire Optical Range for their extraordinary support during these complex experiments.

[48] Janet G. Luhmann thanks the referees for their assistance in evaluating this paper.

References

Borovička, J., and P. Jenniskens, Time resolved spectroscopy of a Leonid fireball afterglow, *Earth Moon Planet.*, *82–83*, 399–428, 2000.

Chu, X., W. Pan, G. Papen, C. S. Gardner, G. Swenson, and P. Jenniskens, Characteristics of Fe ablation trails observed during the 1998 Leonid meteor shower, *Geophys. Res. Lett.*, *27*, 1807–1810, 2000a.

Chu, X., A. Z. Liu, G. Papen, C. S. Gardner, M. Kelley, J. Drummond, and R. Fugate, Lidar observations of elevated temperature in bright chemiluminescent meteor trials during the 1998 Leonid shower, *Geophys. Res. Lett.*, *27*, 1815–1818, 2000b.

Drummond, J., C. S. Gardner, and M. C. Kelley, Catching a falling star, *Sky Telescope*, *99*(6), 46–49, 2000.

Drummond, J. D., B. W. Grime, C. S. Gardner, A. Z. Liu, X. Chu, and T. J. Kane, Observations of persistent Leonid meteor trails, 1, Advection of the "Diamond Ring", *J. Geophys. Res.*, *106*, 21,517–21,524, 2001.

Grime, B. W., T. J. Kane, A. Liu, G. Papen, C. S. Gardner, M. C. Kelley, C. Kruschwitz, and J. Drummond, Meteor trail advection observed during the 1998 Leonid shower, *Geophys. Res. Lett.*, *27*, 1819–1822, 2000.

Jenniskens, P., and R. L. Rairden, Buoyancy of the 'Y2K' persistent train and the trajectory of the 04:00:29 UT Leonid Fireball, *Earth Moon Planet.*, *82–83*, 457–470, 2000.

Jenniskens, P., D. Nugent, and J. M. C. Plane, The dynamical evolution of a tubular Leonid persistent train, *Earth Moon Planet.*, *82–83*, 471–488, 2000a.

Jenniskens, P., M. Lacy, B. J. Allan, D. E. Self, and J. M. C. Plane, FeO "Orange Arc" emission detected in optical spectrum of Leonid persistent train, *Earth Moon Planet.*, *82–83*, 429–438, 2000b.

Jenniskens, P., F. Rietmeijer, N. Brosch, and M. Fonda, (Eds.), *Leonid Storm Research*, Kluwer Acad., Norwell, Mass., 2000c.

Kelley, M. C., et al., First observations of long-lived meteor trains with resonance lidar and other optical instruments, *Geophys. Res. Lett.*, *27*, 1811–1814, 2000.

Kruschwitz, C. A., et al., Observations of persistent Leonid meteor trails, 2, Photometry and numerical modeling, *J. Geophys. Res.*, *106*, 21,525–21,542, 2001.

ReVelle, D. O., and R. W. Whitaker, Infrasonic detection of a Leonid bolide: 1998 November 17, *Meteorit. Planet. Sci.*, *34*, 995–1005, 1999.

Zinn, J., et al., Coordinated observations of two large Leonid meteor fireballs over northern New Mexico, and computer model comparisons, *Meteorit. Planet. Sci.*, *34*, 1007–1015, 1999.

X. Chu, C. S. Gardner, and A. Z. Liu, Department of Electrical and Computer Engineering, University of Illinois at Urbana-Champaign, Urbana, IL 61801, USA.

J. D. Drummond and B. W. Grime, Starfire Optical Range, Directed Energy Directorate, Air Force Research Laboratory, 3550 Aberdeen Ave SE, Kirtland AFB, NM 87117, USA. (jack.drummond@kirtland.af.mil)

T. J. Kane, Department of Electrical Engineering, Pennsylvania State University, University Park, PA 16802, USA.

M. C. Kelley and C. A. Kruschwitz, School of Electrical and Computer Engineering, Cornell University, 304 Rhodes Hall, Ithaca, NY 14853-7501, USA.

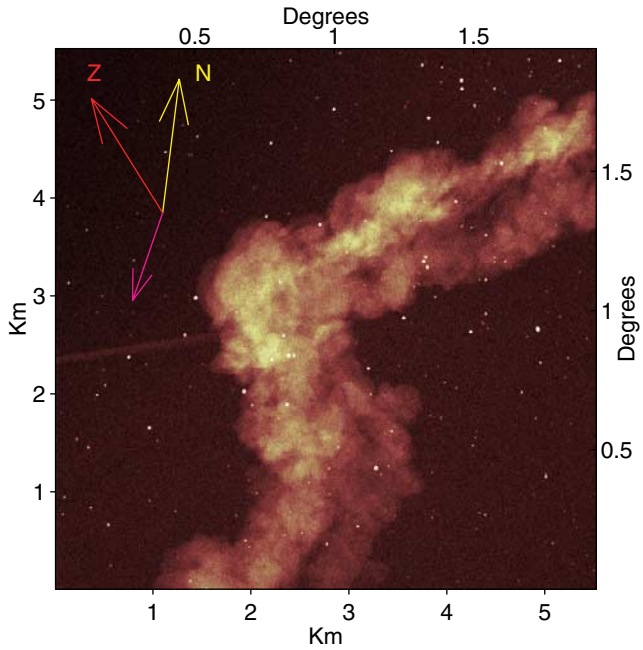

Figure 2. The Glowworm. Ninety four seconds after the appearance of the fireball at 3:05:44 MST, the first one s exposure of its lingering trail was made. The center of the image is directed at an elevation of 33° and an azimuth of 358°. The direction to the zenith and celestial north is indicated, with azimuth increasing to the right, 90° clockwise from the direction to the zenith. The unmarked arrow represents the direction and length of the projection of one kilometer of the initial trail. Barely visible coming in from the left edge is the laser of the 1 watt sodium lidar.